Engineering Science and Technology, an International Journal 38 (2023) 101323

HOSTED BY

Contents lists available at ScienceDirect

Engineering Science and Technology, an International Journal

journal homepage: www.elsevier.com/locate/jestch

Multiparametric experimental analysis of the pin disc rotational cavitation generator

Jurij Gostiša *, Brane Širok, Benjamin Bizjan, Jernej Ortar, Matevž Dular, Mojca Zupanc

Faculty of Mechanical Engineering, University of Ljubljana, Ljubljana, Slovenia

ARTICLE INFO

Article history:
Received 13 September 2022
Revised 15 November 2022
Accepted 28 December 2022

Keywords:
Hydrodynamic cavitation pinned disc reactor
Cavitation dynamics
Flow visualization
Multiparametric analysis

ABSTRACT

The alarming increase in water pollution is driving research into novel, environmentally friendly treatment solutions such as hydrodynamic cavitation. This study is part of the research on the pin disc rotational generator of hydrodynamic cavitation, which utilises the low pressure wake behind the rotor pins to induce cavitation and the short gap between the rotor and stator pins to enhance cavitation cloud fluctuation. Due to the lack of understanding of the effects of cavitation treatment, a laboratory device was built to investigate the mechanisms of cavitation generation and the effects of various geometric features such as the diameter, number, and shape of the rotor pins and the gap size between the rotor and stator pins. Using simultaneously measured pressure fluctuations and high-speed visualisation, a method was developed to quantify the extent of cavitation, and it was found that throttling the high-pressure side had an order- of- magnitude smaller effect on cavitation than the number of rotor pins. It was found that a smaller number of rotor pins with large downstream area produced the most aggressive cavitation conditions. The weak spectral response and lower mean vapour cloud area, as well as the lower fluctuation in the case without stator, demonstrated the key role of the stator in the onset and aggressiveness of cavitation.

1. Introduction

Excessive consumption and production are leading to ever increasing pollution of surface and groundwater, resulting in a worldwide water resource shortage. Overburdened and sometimes outdated wastewater treatment plants (WWTP) are struggling to keep up with novel, potentially toxic compounds entering waterways from ever-changing products. Wastewater is also a major source of a variety of pathogenic microorganisms such as bacteria and viruses [1] that can cause severe infections in organisms that come into contact with the contaminated water, affecting the usability of the water for agricultural use. To make matters worse, antibiotics entering the aquatic environment through WWTP's effluents lead to the emergence of antibiotic-resistant bacteria, which, according to WHO [2], will be one of the greatest threats to human health in the near future. In addition, conventional WWTPs are not designed to simultaneously destroy many structurally diverse micropollutants such as pharmaceuticals and microplastics, as well as pathogenic microbes and viruses, and quickly become inefficient. To follow one of the EU Commission's key actions, it is necessary to develop and research novel technologies capable of removing or reducing pharmaceuticals in WWTPs effluents. Similarly, to prevent new global outbreaks of similar or even more contagious diseases, such as those we are currently experiencing, it is critical to implement technology into WWTPs that could destroy the virus or bacteria before they reach individuals susceptible to infection. Current methods of removing viruses from water are relatively effective, but they are either expensive, time consuming, require a large infrastructure, or more importantly, produce unwanted disinfection byproducts that can be toxic in the long term [3,4]. Of course, there is no doubt that in times of emergency, when human lives are at risk, the cost of effective treatment is not an issue, but when looking at the big picture on a longer time scale, an effective and economically favourable technology is preferable. One such alternative that has proven to be environmentally friendly and economically feasible is hydrodynamic cavitation (HC). HC belongs to the advanced oxidation processes (AOP) is experiencing increasing research interest due to its high treatment potential.

Wang [5], Panda [6], and Yadav [7] have recently reviewed the state of the art in the area of HC, including the review of the devices for HC generation and its scope of application. In order to exploit the hydrodynamic cavitation effects, various types of

* Corresponding author.
E-mail address: jurij.gostisa@fs.uni-lj.si (J. Gostiša).
Peer review under responsibility of Karabuk University.

https://doi.org/10.1016/j.jestch.2022.101323
2215-0986/

Nomenclature

AOP	advanced oxidation process
COD	chemical oxygen demand
HC	hydrodynamic cavitation
RGHC	rotational generator of hydrodynamic cavitation
WW	wastewater
WWTP	wastewater treatment plant

devices can be used to generate cavitation. Passive restriction devices, in which energy is introduced via liquid velocity and pressure include orifice, venturi, and nozzle devices, in which cavitation is generated due to abrupt change in geometry that causes a sudden drop in pressure. These devices are denoted as high energy consuming and therefore, active devices have been introduced where the energy is not required in hydrodynamic form but is supplied by the cavitation generating device itself. Rotating HC generators (RGHC) belong to this category and have been extensively researched by various authors. A dimple rotor device is characterised by a rotor with dimples into which the fluid enters at high velocity. When it exits, low-pressure zone occurs near the indentation causing cavitation. Such devices with a drum-like rotor were investigated by Badve [8], Maršalek [9] (Fig. 1 – A) and a thick disc rotor by Sun [10,11] (Fig. 1 – B). A device in which cavitation is generated in a radial gap between the rotor and stator is studied by Villaroig [12] (Fig. 1 – C) and Cerecedoa [13] (Fig. 1 – D). A serrated rotor–stator device, where cavitation is generated by a high shear field in the axial gap between the rotor and stator teeth, was studied by Širok [14] (Fig. 1 – E), Petkovšek [15,16] (Fig. 1 – F) and Stepišnik [17].

The research on the serrated disc RGHC led to the development of the novel pin disc RGHC with cylindrical pins arranged on the rotor and the stator. Cavitation occurs in the low pressure wake behind the pin on the rotor and has been previously studied experimentally on a pilot scale [18,19] (Fig. 1 – G) and numerically [20]. The pilot scale experimental results indicated significant mechanical and chemical effects that strongly depended on the operational and geometrical RGHC characteristics. The numerical results confirmed the hypothesis that a higher number of rotor pins or a closer spacing between rotor and stator pins did not lead to better performance. This prompted us to build a laboratory-scale RGHC device installed in a test rig that allows experiments to be conducted in a highly controlled environment to evaluate the effects of operational and design features on cavitation characteristics. The study was conducted with the objective of:

1. investigate the mechanisms of HC generation using visualisation and measurement of pressure fluctuations,
2. evaluate the effects of operating conditions and geometric features of the rotor–stator,
3. compare the investigated instances and report good performing features suitable for future implementation.

2. Materials and methods

A test rig was built to evaluate RGHC geometrical features in various operating points regarding their hydrodynamic and cavitation properties. The hydrodynamic properties comprise the pressure and energy characteristics as a function of flowrate, while the cavitation properties were defined by the exerted acoustic pressure fluctuation and visual cloud observation.

2.1. Investigated configuration instances

The study examined several rotor–stator configurations with different geometric features of the protrusions located on the rotor and stator discs, called cavitation elements. The effects of the geometric features investigated in the pilot study [18] dictated the choice of features. These were selected systematically and can be divided into three groups depending on the type of feature. First, the cylindrical rotor pins were varied by number of pins (8, 12 &

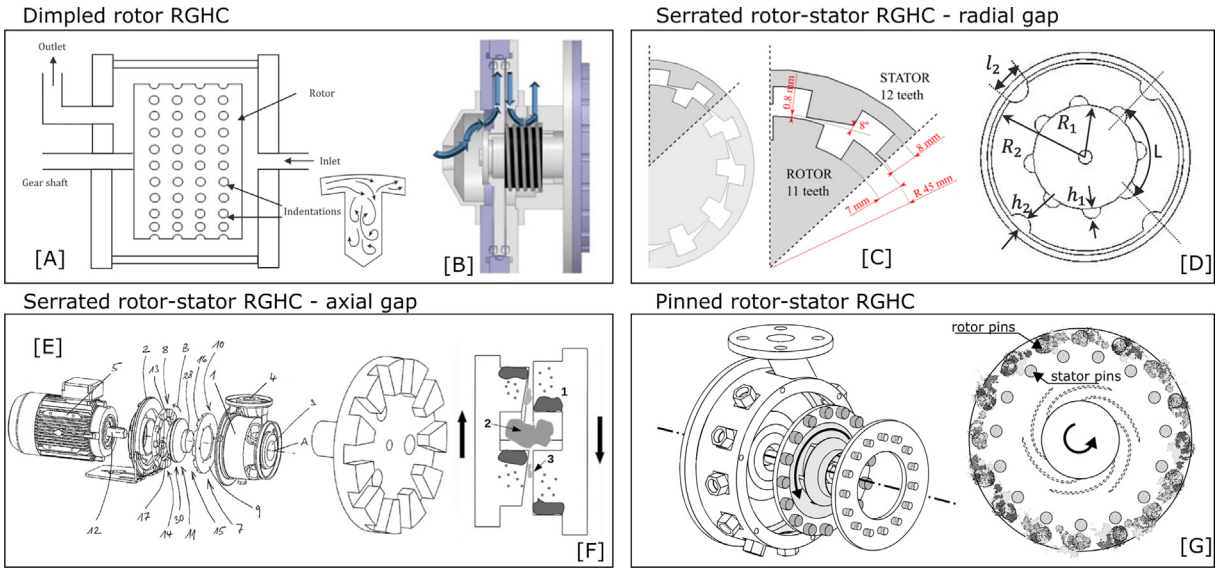

Fig. 1. RGHC device types sorted by the utilized cavitation generation mechanisms. dimpled rotor drum (A) [9] and disc [10], serrated discs with radial gap (C,D) [12,13], serrated discs with axial gap (E,F) [14–17] and pinned rotor and stator discs (G) [18,19].

16) and pin diameter (4 mm, 5 mm & 6.5 mm). The dividing circles with the arranged pins were set to a diameter of 70 mm for the rotor and 55 mm for the stator within the variations. A stator with 15 pins of 5 mm diameter was used in all 9 configurations. Second, the gap distance between the rotor and the stator pins was varied with values 0.25, 1.75 and 4.25 mm and an instance without a stator was added. The only varied feature in this group was the stator disc dividing circle diameter, which was varied with values of 50, 55, and 58 mm. Finally, various non-cylindrical shapes of rotor pins were investigated, such as pointed and blunt triangular, angled pointed triangular, heart shape, and NACA 0500 foil shape. To allow comparison with the cylindrical pins, the nominal cross-section of each shape was set at 5 mm, except for the NACA foil, which used a cross-section of 6.5 mm. All the described configurations are shown in the Fig. 2 (note the direction of rotation marked with an arrow).

2.2. Experimental setup

Due to the rather large number of rotor–stator instances, they were designed in a way to allow simple installation. To investigate the described instances for their cavitation and hydraulic properties, a new RGHC was designed and built to meet the requirements for visualization and pressure measurement in the area where cavitation occurs. Good visualization was expected due to the 2.5D rotor–stator geometry, where the dynamics of the cavitation cloud is expected to be predominantly in the disc plane, which is aligned with the camera view plane. A transparent cover was used to allow the view into the RGHC housing, and a long straight inlet pipe was used to avoid obstructing the view. The newly designed RGHC is shown in the Fig. 3.

A Kollmorgen AKM42J servo motor with AKD-P00606 controller was used to drive the RGHC. The servo motor was selected because of its integrated rotational encoder, which allows very accurate, load-independent adjustment of the rotational frequency. Also supplied with the motor is Kollmorgen Workbench software, which is used to control the motor and record the RMS current, which can be used to calculate torque via the torque constant. A motor with a speed of up to 8000 rpm and a power of 1.5 kW was selected. The motor is coupled to the RGHC rotor via the power transmission unit, which consists of a housing with two bearings and a shaft connected to the motor via a bellow coupling. On the other side, RGHC rotor is fixed on the shaft and the RGHC housing is mounted on the power transmission unit housing.

The RGHC was built into a closed loop system test rig shown in the Fig. 4, with a 5-liter reservoir and a Walter Stauffenberg precision throttle valve, type DV 16 IR. The valve is used to throttle the system on the high pressure side of the RGHC to vary the operating points and simulate the loading that occurs in real systems. Although the system is relatively small, high energy gains are expected due to low hydrodynamic efficiency, resulting in a noticeable increase in fluid temperature. The temperature of the processed fluid was maintained constant using a cooling heat exchanger coil in the reservoir (Fig. 4 – 4) and connected to a Polyscience Durachill CA03 chiller with temperature stability of ±0.1° and cooling capacity of 0.94–1.28 kW at 10 °C – 20 °C.

The requirements of the experiment to describe the hydrodynamic and energy properties of the RGHC determined the selection of the measuring equipment. The pressure head across the RGHC was measured using an Endress & Hauser 2600T 266DSH differential pressure transmitter with a measuring range of −2400–2400 kPa, adjusted to 0–1000 kPa, and total performance of ±0.06 % MR. The inlet pressure is calculated by subtracting the pressure head from the absolute pressure measured with the Endress & Hauser 2600T 264NS. The measurement range of the absolute pressure transmitter is 0.7–600 kPa and the total performance ±0.075 % MR, adjusted by 0.1 % for the age of the transmitter. The flowrate is measured using the ABB ProcessMaster FEP610 DN10 electromagnetic flowmeter with a measuring range of 0–45 l/min and an accuracy of 0.5 % of the measured value. The motor drive and software were used to record the shaft torque and calculate the power.

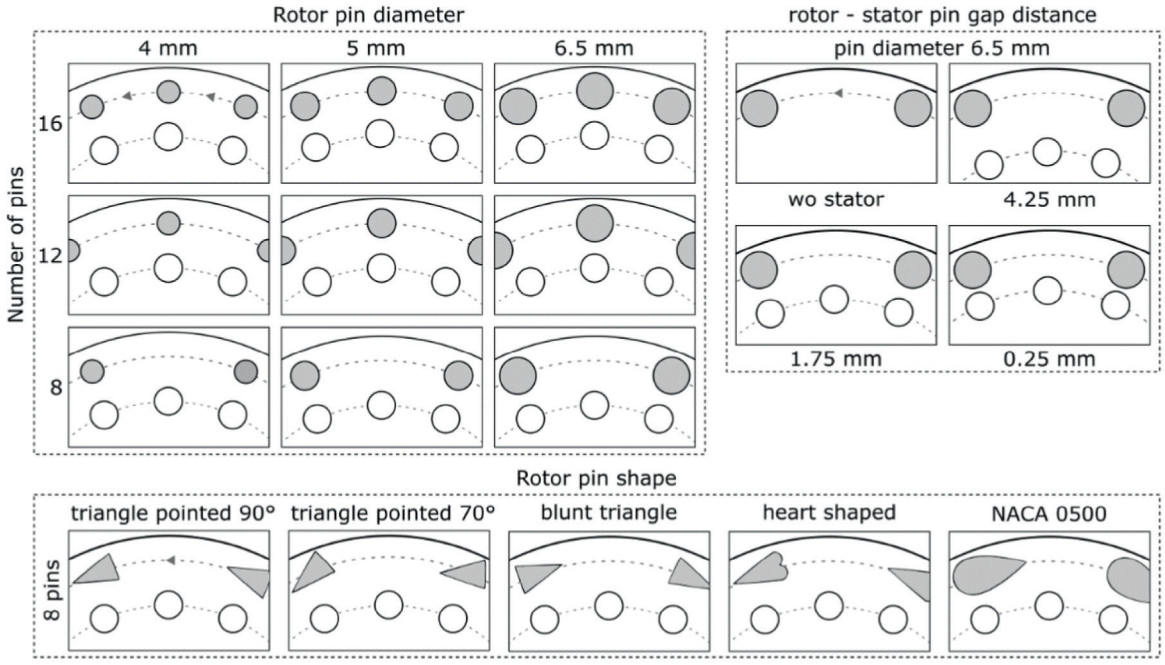

Fig. 2. The three groups of rotor–stator configuration geometry variation: 1 – rotor pin number and diameter variation, 2 – rotor–stator gap distance, 3 – rotor pin shape variation.

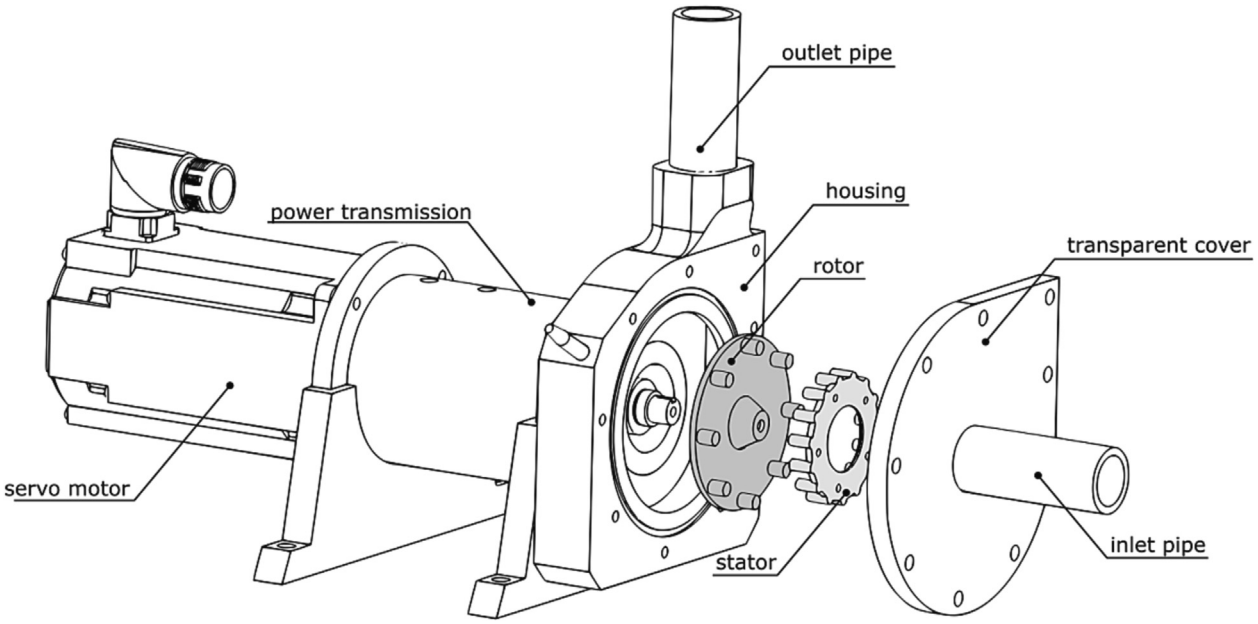

Fig. 3. Exploded view of the newly designed and built RGHC with accompanying power transmission and servo motor.

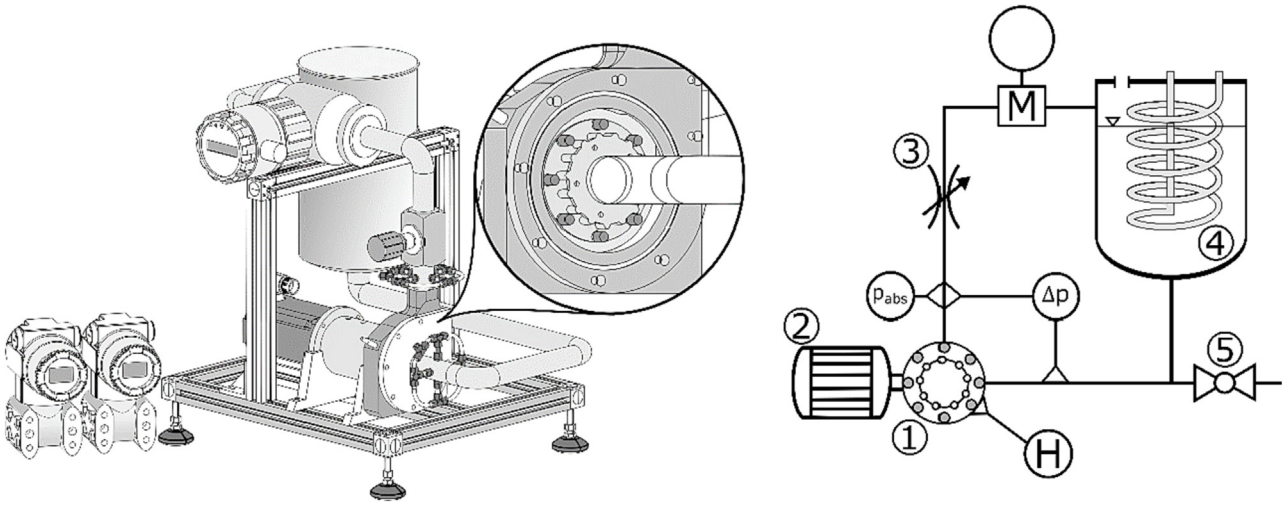

Fig. 4. 3D representation with detail of the RGHC (left) and schematic representation of the measurement rig with marked components (right). 1 – RGHC, 2 – servo drive, 3 – throttle valve, 4 – reservoir with cooling coil, 5 – discharge valve, H – hydrophone, Δ*p* – differential pressure transmitter, p_{abs} – absolute pressure transmitter, M – flowmeter.

3. Experimental design

An experiment was designed to investigate the 17 rotor–stator configurations for their hydrodynamic properties over a wide operating range and cavitation characteristics at three operating conditions. The first part of the study includes the measurement of hydrodynamic and energy characteristics while the second part includes the characterization of cavitation. Each rotor–stator configuration was tested at same rotational frequency and flow rate, hence inlet pressure.

3.1. Hydrodynamic characteristics

To evaluate the hydrodynamic properties of each configuration, the pressure and energy characteristics of each configuration were measured with respect to the flowrate in 10 operating points. The rotational velocity was set at 7000 RPM and the operating points were set using the throttle valve at the RGHC outlet. Visually, 17 rotor–stator characteristic curves would be difficult to compare, so 3 operating points at flowrates 8, 16 and 24 l/min were selected for comparison. Cavitation number is a function of operating point, as it depends on suction side pressure, vaporisation pressure, and rotational velocity. The last two were constant and the suction-side pressure is a function of the flowrate and suction-side pipeline friction coefficient. While the coefficient is a material property of the inlet pipe, the cavitation number depends directly and solely dependent on the flowrate. Since only the rotor and stator are varied in the study, and the pipeline is not, the cavitation number is the same for the compared configurations at each operating point.

3.2. Cavitation characteristics

The second part of the study aimed to characterise the cavitation conditions for each rotor–stator configuration at the 3 operat-

ing conditions described. The objective of the study was to identify and quantify the predominant mechanisms of cavitation generation and cloud shedding. To this end, acoustic pressure time series recorded with the hydrophone and image data acquired with the high-speed camera were used. The data were acquired synchronously to investigate the effects of cloud dynamics on the pressure fluctuation. The pressure time series was transformed to the frequency domain to determine the main contributions to the fluctuation dynamics. RMS values were used to compare mutual instances and operating points. The hydrophone and camera were positioned as shown in Fig. 5.

The camera was aligned with the rotor axis and positioned to capture the image in the plane of the rotor disc. The angle of view was adjusted to cover a large area of interest that allowed a long, continuous time series of the pin path to be recorded, but not too wide to preserve high image resolution and allow clear separation of the cavitation cloud from the background. The tracked path of the rotor pin should be as long as possible in order to investigate the expected low-frequency fluctuations due to the rotor–stator-pin interaction. The cavitation cloud in the rotor–stator region was captured at 150,000 frames per second at a resolution of 384 × 256 px using the high-speed camera FASTCAM SA -Z, type 2100 K-M-64 GB with 12-bit grayscale sensor. Diffuse and uniform illumination was used to achieve high contrast and good visual separation of the cloud from the background. Raw high-speed video material is provided in supplementary data. The acoustic pressure emission was recorded using Teledyne Reson TC4013 hydrophone and EC6081 preamplifier. The signal from the preamplifier was acquired using the National Instruments NI9174 cDAQ chassis and NI9222 DAQ card and sampled at 300 kS/s. The image and pressure acquisition were synchronised with the trigger signal from the camera, which was acquired by the same DAQ card and recorded using software created in Labview. Image processing algorithm.

Image processing was performed with a self-developed algorithm written in Labview using the IMAQ VI library. Before the execution of the cloud identification algorithm was executed, the image transformation to the rotating reference frame was performed. The part of the image behind the pin is extracted and rotated around the centre of the disc rotation with exactly the same rotation speed in the direction opposite to the disc rotation. This was made possible by the extremely high rotational frequency accuracy and stability of the servo drive with its built-in precision rotational encoder. The encoder, with a resolution of 20 bits and an accuracy of 0.6 arc minutes, is connected to the drive controller in a feedback loop that ensures an accuracy of the set rotation speed of more than 0.01 %. The transformation eliminated the relative rotational motion of the pin so that the description of the cloud dynamics is independent of the rotation of the disc. The Fig. 6 shows an example of the image transformation and the identification of the cavitation cloud.

The algorithm has been applied with same parameters to all cases in question and was found to give accurate results, based on a qualitative evaluation with the identified cloud contour overlayed over the raw captured image as shown in the Fig. 6. Processed image sequences of each configuration instances are provided in supplementary data. After the image transformation, the algorithm was applied in the sequence as stated:

1. the starting point represents raw captured image trimmed to the area behind the pin and transformed into the rotational reference frame, further on denoted as A_i.
2. Region of interest is masked – pin, outside rotor area and inside stator area are masked out.
3. Background image is calculated by multiple image averaging (approx. 3000images) and subtracted from the processed image using the flat field correction VI [21], where mean image was used as the flat field image:

$$A_{flatfield} = \frac{1}{N}\sum_{i=1}^{N} A_i,$$

$$A_{corr} = \frac{(A_i - A_{darkfield}) \cdot median(A_{flatfield} - A_{darkfield})}{(A_{flatfield} - A_{darkfield})} \cdot k,$$

where A_{corr} is the corrected image and A_i is the input image. Dark field Image $A_{darkfield}$ is the image that captures the dark currents in the sensor, flat field Image $A_{flatfield}$ is the image intensity profile image, and the correction factor k is a constant to bias the brightness of the corrected image. For the calculations, an image with

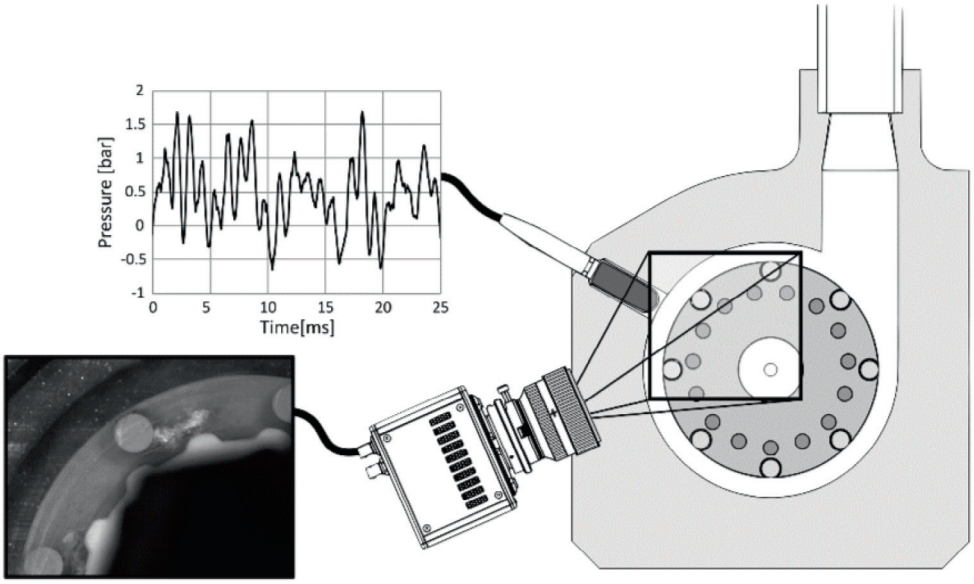

Fig. 5. Schematic representation of camera and hydrophone positioning.

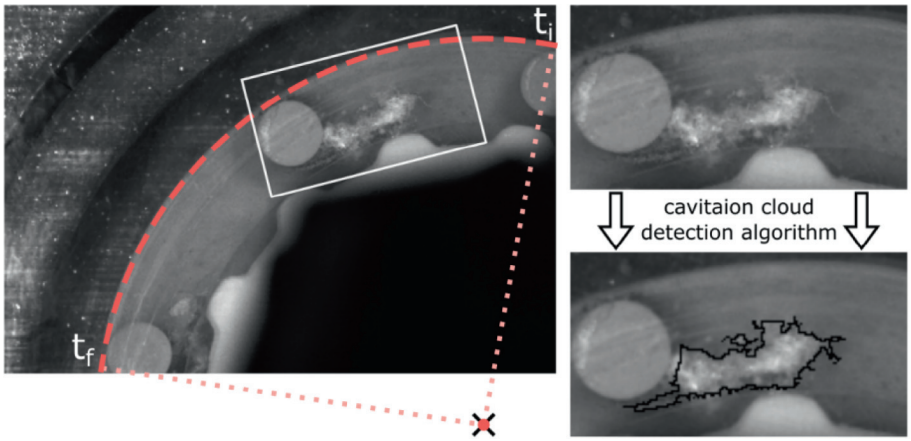

Fig. 6. Example of image transformation and algorithmically identified cavitation cloud.

the camera lens covered was used as the dark field image and correction factor of 1 was used.

4. Edge detection filter using the Sobel method [22] with the default threshold value (0). The Sobel operator is based on convolving the image with a small, separable, and integer valued filter in horizontal and vertical direction. Mathematically, the operator uses two 3 × 3 kernels which are convolved with the original image to calculate approximations of the derivatives – one for horizontal and one for vertical change in the greyscale value. For the source image A, the images G_x and G_y contain at each pixel the horizontal and vertical derivative approximations:

$$G_x = \begin{bmatrix} +1 & 0 & -1 \\ +2 & 0 & -2 \\ +1 & 0 & -1 \end{bmatrix} * A \text{and } G_y = \begin{bmatrix} +1 & +2 & +1 \\ 0 & 0 & 0 \\ -1 & -2 & -1 \end{bmatrix} * A,$$

where * operator denotes the 2-dimensional convolution signal processing. The origin of the coordinate system is set to top left corner of the coordinate system and x direction defined as increasing towards right, and y increasing towards bottom. Each image pixel can be expressed as gradient magnitude, combining the resulting gradients:

$$G = \sqrt{G_x^2 + G_y^2}$$

5. Image is binarized with the thresholding condition "greater than 0".
6. Fill hole morphological operator is utilized to fill the holes inside the cloud. The cavitation cloud is treated as a uniform entity as only total cloud area is found relevant.
7. Remove particle filter VI [21] is used to remove small parts of the cloud with the default number 2 of 3 × 3 erosions applied to the image.
8. The initial image is overlayed with the identified cloud contour to qualitatively evaluate the accuracy of the algorithmically determined cloud shape. (Figs. 6 and 7-7). Under all operating conditions, overlayed cloud area was found to be in a good agreement with the visible area in raw images.

4. Results and discussion

The results are shown in three parts. The first one is dedicated to the results of integral hydrodynamic properties measurements and the second one to local fluid dynamics its relation to the cavitation phenomena. The last part comprises of the rotor–stator configuration comparison in terms of hydrodynamic and cavitation properties.

4.1. Integral hydrodynamic properties

The pressure and energy characteristics of each rotor–stator configuration were measured. The characteristic curve represents the pressure head, energy, and inlet pressure as a function of flow rate. The pressure head represents the difference measured with the differential pressure transmitter (marked Δp Fig. 4). To obtain the inlet pressure, the measured pressure difference was subtracted from the value measured with the absolute pressure transmitter at the RGHC outlet. The adjusted power P_A represents the mechanical shaft power, reduced by the drive losses, which occur mainly due to the friction losses of the mechanical seal and add up to 263 W. The inlet pressure was calculated as $p_{in} = p_s - \Delta p$ (Fig. 4). For better visual representation, a linear curve was fitted over the pressure and adjusted power values and a second-order polynomial curve was superimposed over the inlet pressure values. Examples of the characteristics for the 8 pin 6.5 mm instance are shown in Fig. 8, while the rest are provided in the supplementary data.

The measured characteristics exhibit features typical of centrifugal-type turbomachinery, where energy consumption is proportional and pressure head is inversely proportional to flow rate. The pressure head is a direct measure of the pumping ability, while the consumed energy is converted into hydrodynamic energy of the transported liquid or dissipated in various ways, as in this case by cavitation generation. For illustration, the hydrodynamic efficiency $\eta_H = \frac{\Delta p \cdot \dot{V}}{P_A}$ of the RGHC example in Fig. 8 is about 5 % at the lower and 15 % at higher flow rates, while the remaining portion of the energy is dissipated via mechanisms such as turbulence and cavitation. It is important to note that the desired main effect of the RGHC is cavitation, while the pressure head is not. The deviation of the linear curve shape from the typical second-order polynomial shape of the pressure characteristic of a centrifugal pump is mainly due to the shape of the rotor. The pins do not resemble the typical centrifugal pump vanes, which form the inter-blade channels where losses occur proportional to the square of the flow rate [23]. Furthermore, it is well known that the pressure characteristics of the pump drops suddenly at the onset of cavitation, and the developed cavitation is present throughout the operating range of the RGHC.

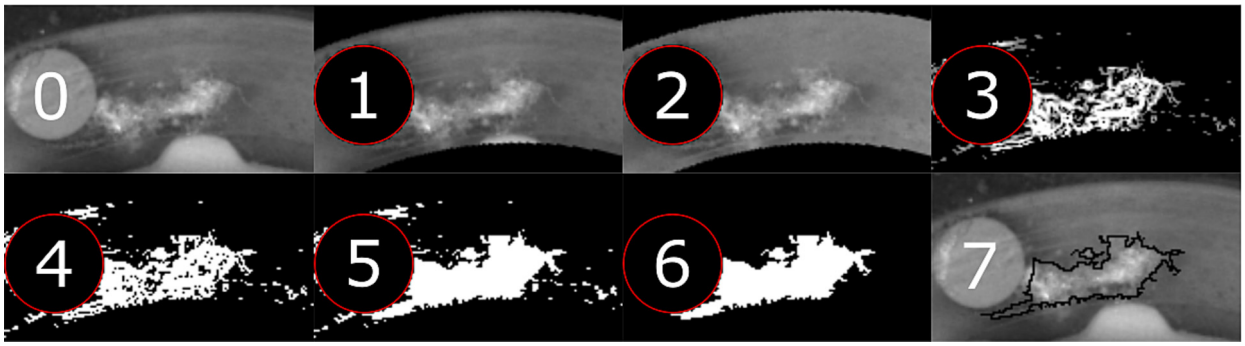

Fig. 7. Cloud detection algorithm sequence. 0 – initial image; 1 – masking; 2 – background subtraction; 3 – Sobel edge detection; 4 – binarization; 5 – fill hole filter; 6 – particle remove filter; 7 – cloud contour overlay.

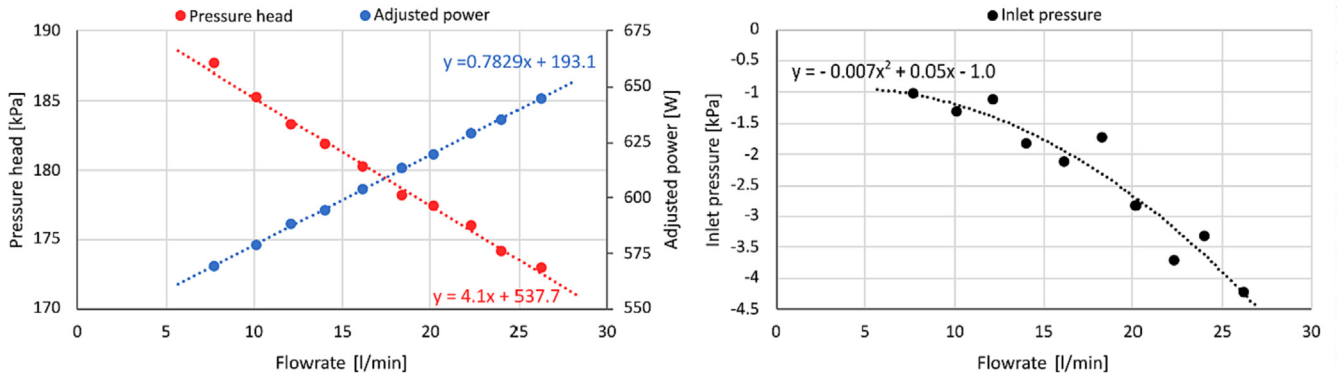

Fig. 8. 8 pin 6.5 mm pressure and adjusted power characteristics (left) and inlet pressure curve (right).

The inlet pressure depends solely on the pressure drop in the inlet pipeline, which is proportional to the velocity squared and the coefficients of friction [23]. While the coefficients are related to material properties, the pressure is directly proportional to the flow rate. A higher flow rate results in a higher pressure drop in the inlet pipeline and thus a lower pressure at the inlet of the RGHC. The inlet pipeline remains intact during rotor–stator variation and so does the inlet pressure and cavitation number for all configuration instances at each operating point. The cavitation number was calculated as $\sigma = \frac{2(p_{in}-p_v)}{\rho v^2}$ where p_{in} is the inlet pressure and p_v is the water vaporisation pressure at 20 °C (2339 Pa). The constant temperature is allowed by the strict temperature control with the chiller and the exchanger in the reservoir. Velocity v was calculated as the circumferential velocity of the pin $v = \pi dn$ where d is the pin dividing circle diameter and n is the rotational speed of the rotor, thus σ was independent of the pin shape. As listed in Table 1, it was found that the cavitation number was not significantly affected by the high pressure side throttling.

Another dimensionless parameter important for characterization of local flow conditions is Reynolds number defined as $Re = vS\rho/\mu$, where v is pin circumferential velocity, S is characteristic pin size and μ = 0.001 Pa•s is water viscosity at 20 °C. In the case of circular pins, S was equal to pin diameter. For non-circular pins, S was equal to 5 mm, with the exception of NACA pins where S = 6.5 mm was considered. This means only three different characteristic pin sizes were used, namely 4 mm, 5 mm and 6.5 mm. Corresponding Reynolds numbers were $1.03 \cdot 10^5$, $1.28 \cdot 10^5$ and $1.67 \cdot 10^5$, respectively. Therefore, cavitating flow in the pin region was highly turbulent under all operating conditions.

Table 1
The three operating points with the flow rates, inlet pressures and accompanying cavitation numbers.

Flowrate [l/min]	8	16	24
Inlet pressure [kPa]	−0.5	−2.0	−3.5
Cavitation number	0.299	0.295	0.290

4.2. Local cavitation properties

The acoustic pressure emission recorded with the hydrophone and the high-speed visualization of the cavitation phenomenon were used to describe the local cavitation properties. The effects of RGHC operating parameters on cavitation and other flow characteristics are evaluated using power spectra of the pressure time series (each 1 s long) recorded with the hydrophone. The flowrate throttling did not have a noticeable effect on the power spectra shape, indicating a robust nature of the device, suitable for installation in the systems with increased hydrodynamic loads. The first parameter studied is the number of rotor pins for a 6.5 mm diameter round pin. The corresponding power spectra (FFT) are shown in Fig. 9 for rotors with 8, 12 and 16 pins. Several distinct amplitude peaks can be seen in the spectra. The first discrete peak occurs at 116.7 Hz and results from the rotation of the rotor as it coincides with the rotor's rotational speed of 7000 RPM. Similarly pronounced peaks occur at pin-pass frequencies of 933, 1400, and 1866 Hz for the 8, 12, and 16 pin instances, respectively, and correspond to the frequency of the rotor pins passing through the hydrophone (rotational frequency multiplied by the number of pins). In the 8 and 16 pin instances, second pin-pass harmonics are visible at 1866 and 3732 Hz.

For all instances, except the one without stator, a broader amplified band occurs between 500 and 1000 Hz due to cavitation

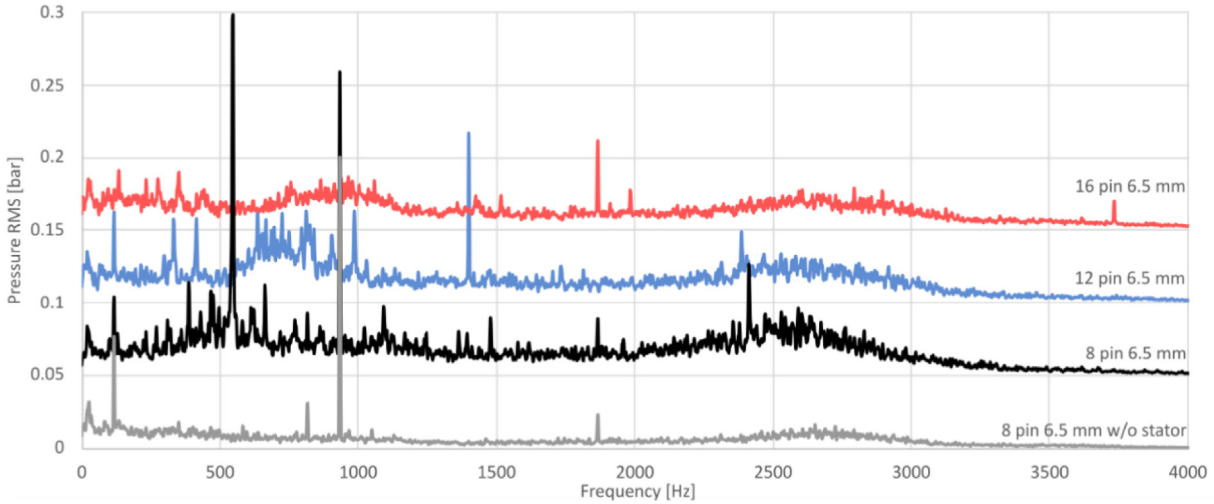

Fig. 9. Power spectra of 6.5 mm pin instances with 8, 12 and 16 pins and the instance without the stator.

cloud shedding in the Karman vortex street behind the rotor pin, which is amplified by the interaction of the rotor and stator. As noted by Gostiša et al. [18], the shedding frequency imposed by rotor–stator passages may prevail over naturally occurring shedding frequency (i.e., cylinder in free flow). It is difficult to identify the contributing stator feature because there are 15 relatively large stator pins that significantly narrow the flow path, and no corresponding frequencies are observed. Nonetheless, the instance without a stator significantly differs from the others by the overall lower fluctuation, while only amplified rotational and pin-pass frequencies are visible.

In the 8-pin case, a distinct peak is observed at 547 and 2412 Hz, which cannot be attributed to a geometric feature combined with the set rotation frequency, nor to vortex shedding, since the peak is very narrow. It could be due to a pronounced resonant frequency of the housing chamber, which will be investigated in a future study by varying the volume of the chamber. Nevertheless, the amplified frequencies and their correlation to cavitation-related phenomena were investigated using simultaneous imaging. A typical example of the pressure time series and cavitation cloud area are shown in Fig. 10.

As shown in the numerical study of the pin disc RGHC [20], the result of cavitation is a complex pressure–velocity field, which is also evident in the dynamics of the acquired pressure signal. While some of the dynamic features can be attributed to the geometric features and the rotational frequency, there are others such as 547 Hz that can be linked to the dynamics of the cavitation cloud detachment and collapse. A such typical event of cloud inception, growth and detachment is shown in the image series in the Fig. 10 (for more examples refer to the videos in supplementary data). The area observed with the high-speed camera is approximately a quarter of the chamber, which hinders the recording of longer cloud area time series and makes it difficult to directly correlate the cloud area and acoustic pressure time series. Nevertheless, there is a strong overlap of the cloud average and 547 Hz sine that links the cloud collapse and the increased pressure fluctuation at the given frequency (Fig. 9 – 8 pin 6.5 mm). Moreover, an increased spectral peak occurred at 2.4 kHz, which has a strong influence on the shape of the pressure time series as seen in the time series comparison in the Fig. 10. The latter is attributed to multiple cloud bursts that occurred simultaneously behind several rotor pins, causing pressure perturbations that propagated throughout the housing chamber. This phenomenon was to some extent observed in the [20] and will be further experimentally investigated using a wider viewing angle to capture dynamics of entire chamber.

The basic mechanism of vortex shedding on a moving cylinder is Karman's vortex street, in which vortices of single- or multiphase fluid (in the case of a cavitating flow) structures periodically develop and detach from the cylinder surface [24]. Assuming a Strouhal number of St = 0.2 (a typical value occurring in a wide range of Reynolds numbers), the shedding frequency $f_s = \frac{St \cdot v}{d}$ in the near-wake of the pins with 6.5 mm diameter can be estimated to 992 Hz [25]. Note that this frequency is a rough estimate that may differ by about ±10 % from the actual shedding frequency due to the unknown exact value of the Strouhal number and the fact that the water flow past the pin also has a radial velocity component that has not been measured. Since the estimated shedding frequency is also close to the pin passage frequency of 933 Hz, this could be the reason why it is not visible as a distinct peak in the spectrum. However, as we have observed in our previous studies [18], the rotor–stator interaction can enforce a higher frequency and intensity of the attached cavitation clouds collapses than would occur in the pure Karman shedding mechanism (i.e., without the influence of the rotor–stator interaction). For better representation see the associated visualization data in the supplementary. This is also the case in the present study, as all spectral peaks have much lower amplitude when the stator is removed. In addition, there appears to be much less broadband noise between 500 and 1500 Hz in the arrangement without the stator, where spectral peaks are expected to arise from forced vortex shedding (induced by rotor–stator interaction). These results confirm the key role of the stator in generating intense hydrodynamic cavitation in the pinned disc reactor.

Another design parameter that significantly affects the cavitation dynamics is the shape of the rotor pins (Fig. 11). Regardless of the shape of the pins, the amplified discrete rotational frequency and its second harmonic are visible at 116.7 Hz and 234 Hz, respectively. In addition, the discrete peak of rotor passage for 8-pin rotors occurs at 933 Hz and the second harmonic at 1866 Hz is smeared but also visible. However, the shape of the spectrum in the 500 Hz region depends largely on the shape of the pins. Compared to other pin shapes, circular and triangular pins produce a much higher spectral response, including several peaks most likely related to cavitation cloud dynamics and rotor–stator interaction. Heart-shaped and triangular pins pointed 90° have a similar shape

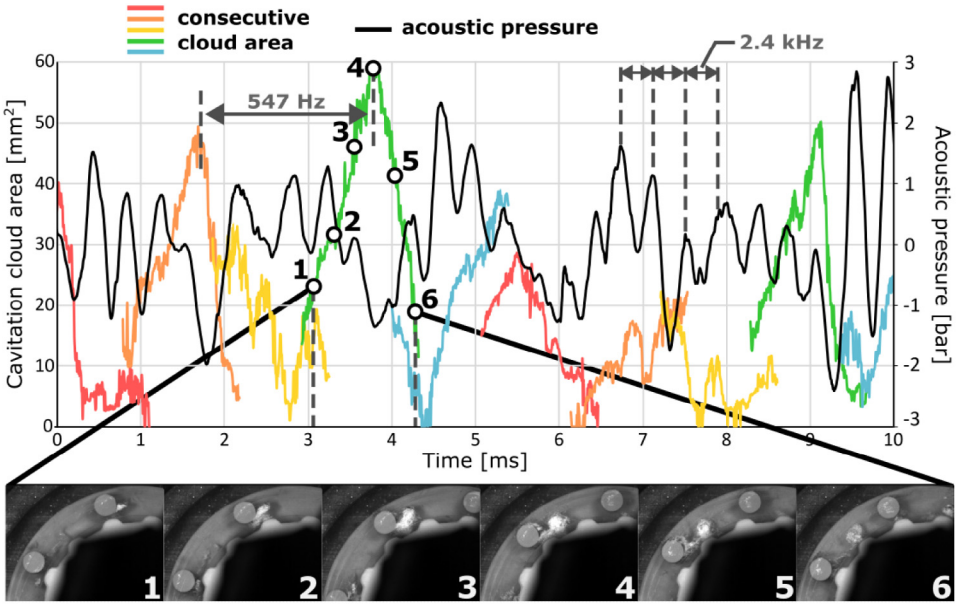

Fig. 10. Synchronized time series of hydrophone pressure (black continuous curve) and cavitation clouds area (coloured curves representing consecutive clouds).

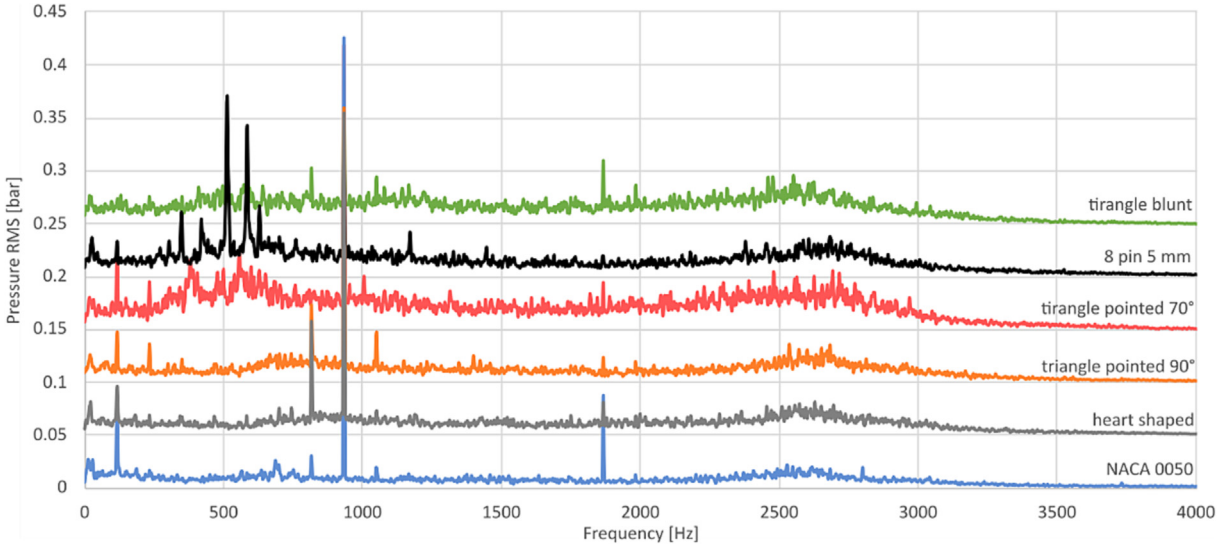

Fig. 11. Power spectra of the pin shape variation instances.

and therefore exhibit a similar spectral response. In the case of NACA 0500, the dynamics of the cavitation cloud is significantly lower, as indicated by the absence of peaks in the band around 500 Hz.

4.3. Rotor-stator configuration instance comparison

For the rotor–stator configuration comparison, the pressure head and adjusted power input were used to quantify the hydrodynamic properties of the RGHC, and acoustic pressure emission, cloud area average and standard deviation were used to evaluate the extent of cavitation and its dynamic properties. Results in this section are provided for three different water flow rates (corresponding cavitation numbers and inlet pressures are provided in Table 1).

5. Pressure head and power consumption

As expected for a centrifugal type of a turbomachine, the pressure head increases and the power consumption decreases with increasing throttling (reduced flow rate). Although the cavitation elements do not resemble the geometry of a pump vane, the ability to generate head is significant. Looking at the graphs in Fig. 12, the following trends can be observed:

→ As shown in Section 4.1, the pressure head is proportional to the number and diameter of the pins in all cases. Although the cylindrically shaped pins serve as poor pump vanes, an increase in the number and diameter leads to an increase in the surface area in contact with the fluid, which allows for a greater transfer of mechanical to hydrodynamic energy. This is also shown by the fact that the power consumption is proportional to the number and diameter of the pins.

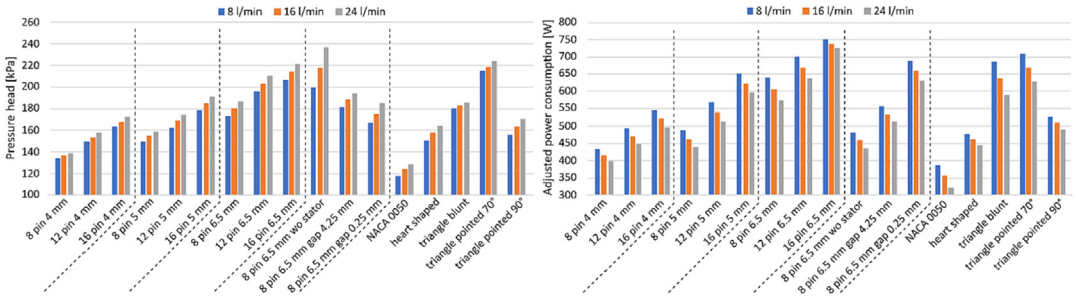

Fig. 12. Pressure head (left) and adjusted power consumption (right) instance-operating point comparison.

→ The highest pressure head and thus pumping ability is achieved with the triangular pins pointed 70°, where the cavitation elements are shaped as isosceles triangles inclined at an angle of 70° to the tangent line of the pin dividing circle. This instance shape most closely resembles the backward-curved pump vanes normally found on a centrifugal pump impeller. Further on, the height and slope of the triangle can be changed to meet the desired pressure requirements.

→ NACA05000 has the lowest pressure head with the lowest energy consumption, which is due to the lowest drag coefficient of the foil shape.

→ The stator can be considered as a throttling element, reducing the pressure head and increasing the energy consumption. This is most evident in the case without the stator, where the pressure head is about 15 % higher and the energy consumption is about 25 % lower than for the 8 pin 6.5 mm instance with a 1.75 mm gap. A decreasing trend in pressure head is observed with shorter gap distance. Stator design features are to be investigated in a further study.

6. Pressure fluctuation

As shown in the previous chapter and in [20,24,25], pressure fluctuations are highly correlated with the cavitation onset. Therefore, the effective pressure value was used to compare the instances at the three operating points in terms of the cavitation extent and is shown in Fig. 13.

As with the pilot study [18], where throttling the high pressure side did not result in favourable cavitation conditions, it can be seen that the effective pressure decreases with increasing throttling. Nevertheless, the throttling did not suppress the effective pressure significantly, indicating a robust nature of the RGHC, which is an important information to consider when designing the installation in the system. Regarding the effects of geometrical characteristics on the effective pressure values, the following conclusions can be drawn:

→ Larger pin diameter causes larger-scale pressure fluctuations and thus a higher effective pressure value. Namely, in accordance with hydrodynamic drag law $F_D = 0.5\rho c_D A v^2$, the larger cross-sectional area leads A to a higher drag force F_D between the front and the back side of the cavitation element (pressure difference across pin acting over a larger area). Consequently, the hydrophone -measured effective pressure value is increased.

→ Higher number of pins leads to a lower effective pressure value. Similar results were previously found in pilot and numerical studies [19,21], where the pilot device with more pins resulted in lower chemical oxygen demand (COD) reduction and the numerical results showed lower cavitation extent and effective pressure value. In the numerical study [21], the impeded development of the cavitation cloud was attributed to a reduced low-pressure wake region downstream of the cavitation element, which prevents cloud elongation and shedding.

→ The highest effective pressure values are exerted by triangular pins inclined 70° and 8 pins with 6.5 mm diameter. These are each characterized as particularly aggressive in terms of cavitation, as indicated by high pressure fluctuations.

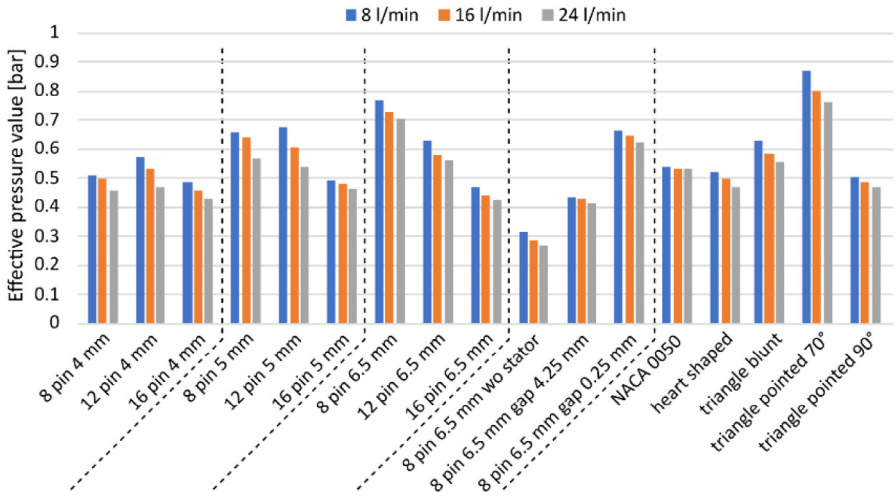

Fig. 13. Effective pressure value instance-operating point comparison.

→ The lowest effective pressure is obtained in the configuration without stator. Therefore, the stator is one of the key elements of the RGHC that induces the desired fluctuation and enables the aggressive cavitation conditions.
→ It was found that shortening the rotor–stator gap difference increases the RMS pressure value up to a certain point. The effective pressure value is lowest in the case with 4.25 mm gap, while it is higher in the case with 1.75 mm than in the case with 0.25 mm, indicating the existence of the optimal gap distance.

7. Vapor cloud characteristics

The area of the vapor cloud was determined using the algorithm presented in the chapter 3.2.1. To compare the cloud properties of each rotor–stator instance, the standard deviation and area average were used. The standard deviation shows the variation in cloud area size, with a higher value being considered favourable and indicating more aggressive cavitation (will be further investigated on contaminated samples), while the area average of the cloud indicates the overall extent of cavitation. Even before looking at the bar trends, a significant similarity of the standard deviation of the cloud area to the effective pressure value is observed, indicating a significant mutual influence of cloud shedding on the pressure variations. The high correlation of pressure and cavitation dynamics makes acoustic pressure measurement an effective tool for evaluating the extent of cavitation in many cases where visualization is not possible (see Fig. 14).

The standard deviation of the cavitation cloud area shows a similar trend as the effective pressure:

→ decreasing cloud area deviation with increasing high pressure side throttling,
→ decreasing cloud area deviation with increasing pin number,
→ increasing cloud area deviation with decreasing rotor–stator gap, including the occurrence of the inflection point and the maximum value for the gap 1.75 (example 8 pin 6.5 mm),
→ good performance of the instances triangle pointed 70°, 8 pin 6.5 mm, 8 pin 5 mm and poor performance of the configurations with 4 mm pins, 16 pins, NACA0500 and the one without stator.

The cloud area was found to increase with larger pin diameter and decrease with greater pin number, where particularly high pin numbers seem to have a significant reducing effect. The cavitation- suppressing effect of a higher pin number is consistent with the findings of [20], which attribute the mechanism of cavitation generation to the low pressure wake behind the moving pin. When the pins are placed too close to each other, the formation of the low pressure wake is unlikely due to the small area behind the pins and cavitation occurs to a much lesser extent and with far weaker dynamics (no cloud elongation and collapsing). This is observed for all 16 pin instances regardless of pin diameter.

The highest average cloud area average is observed with the blunt triangles, which is due to the constant presence of the cavitation cloud behind the front triangle face, as can be seen in Fig. 15. Despite the presence of the cloud for longer periods of time, the fluctuation is lower compared to the cases with 8 pin 6.5 mm and triangle pointed 70° (see Fig. 14).

8. Regression models of integral RGHC parameters

To quantify our observations from the previous sections, the following integral parameters related to the RGHC's performance were modelled by fitting to measured data:

- root-mean-square value of the hydrophone pressure (p_{RMS}),
- average cavitation cloud area (A_{AVE}),
- standard deviation of cavitation cloud area (A_{STD}).

These parameters were be modelled by a power law fit to their measured values according to Eq. (1):

$$C = a_0 \cdot N^{a_1} \cdot d^{a_2} \cdot Q^{a_3} \tag{1}$$

where C is the modelled parameter of interest (any of the three above specified), N is the number, d is the diameter of rotor pins, respectively, and Q is the volumetric flow rate of water. N, d and Q are independent variables to which p_{RMS}, A_{AVE} and A_{STD} were fitted. By performing a least-squares power law fit, the following models were obtained:

$$p_{RMS} = 0.589 \cdot N^{-0.379} \cdot d^{0.326} \cdot Q^{0.118} \tag{2}$$

$$A_{AVE} = 167 \cdot N^{-1.658} \cdot d^{0.171} \cdot Q^{0.192} \tag{3}$$

$$A_{STD} = 89.2 \cdot N^{-1.175} \cdot d^{-0.161} \cdot Q^{0.180} \tag{4}$$

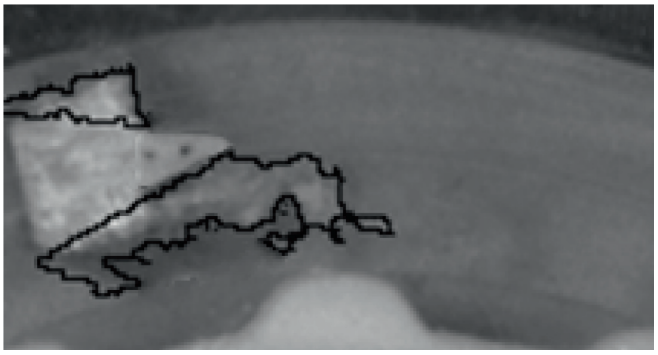

Fig. 15. Typical cavitation structure behind the blunt triangle rotor pin, present over longer time periods and not fluctuating heavily.

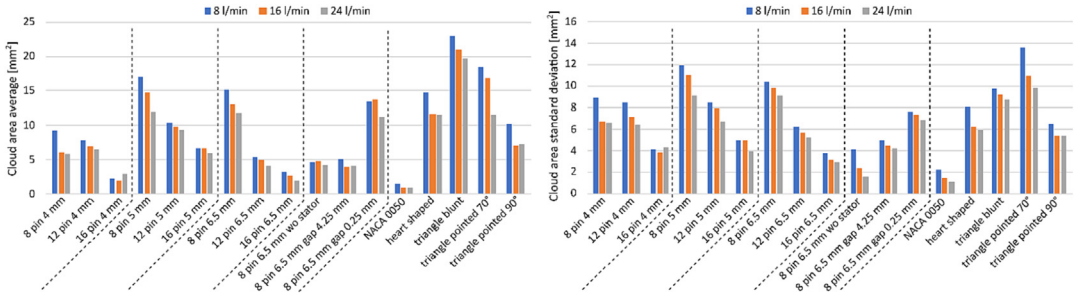

Fig. 14. Cavitation cloud average area (left) and standard deviation (right) instance-operating point comparison.

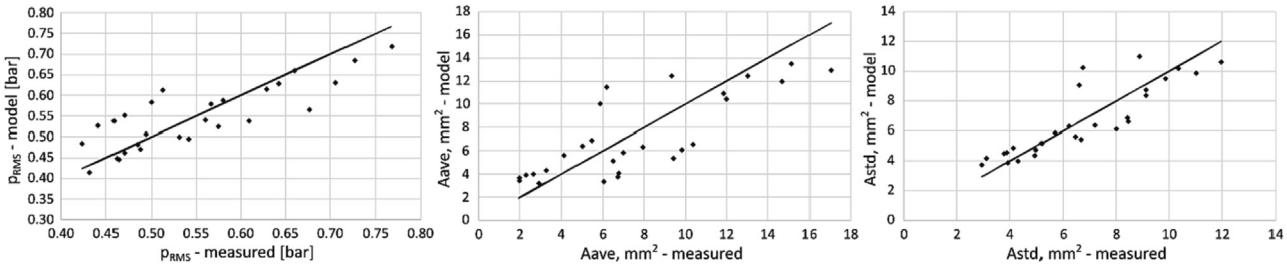

Fig. 16. P_{RMS}, A_{AVE} and A_{STD} regression models.

Goodness of fit in Eqs. (2), (3) and (4) can be assessed from diagrams in Fig. 16, where measured and modelled parameter values are compared. Due to a few outliers in each model, the R^2 value is relatively low, although the majority of predicted values is in a reasonably good agreement with the measured values not deviating by more than 15 %. For this reason, proportionalities given by Eqs. (2)–(4) still express a valid trend. As suggested by these equations and consistent with our previous comments of measured integral RGHC parameters, cavitation intensity proportional to (p_{RMS}, A_{AVE} and A_{STD}) is decreasing rapidly (note the large a_1 exponent value, particularly in cloud area regression models) as the number of rotor pins increases. Particularly the optically measured local cavitation cloud area (i.e. observed on a single pin) and standard deviation thereof (A_{AVE} and A_{STD}, respectively) have a strong negative correlation with the number of pins. This is likely due to the obstruction of the flow field and low pressure wake by closely spaced pins. If N is sufficiently low, each pin moves in a free flow field and the maximum cavitation intensity on the pin can be achieved. A decrease between N = 8 should be further investigated and the number at which A_{AVE} and A_{STD} starts to decrease should be determined. The fact that the value of the exponent a_1 is only −0.379 for p_{RMS} but over 1.1 for A_{AVE} and A_{STD} suggests that pressure fluctuations measured with the hydrophone are only partly caused by the collapse of cavitation structures, while also come from other significant sources such as the intermittent gap flow as the rotor pins pass the stator pins. Rich dynamics of the exerted pressure is the result of simultaneous interaction of all rotor and stator pins.

With respect to the pin diameter, p_{RMS} and A_{AVE} increase slightly with d, also indicating a more intense cavitation and larger pressure fluctuations induced by the gap flow, as the rotor–stator gap becomes smaller. Nevertheless, A_{STD} is observed to decrease, possibly due to the overall larger cloud area and volume that makes partial collapses of vapor structure less visible (although not necessarily less potent, as suggested by the trend that p_{RMS} increases proportionally $d^{0.171}$). Finally, the liquid flow rate also appears to have a slight positive effect on the cavitation intensity, as all three related parameters (p_{RMS}, A_{AVE} and A_{STD}) increase with Q, which is in agreement with the previously noted small impact of high pressure side throtling. This is consistent with decreasing cavitation number (Table 1). Having said that, the pin diameter and liquid flow rate have a less significant cavitation intensity effect compared to the number of pins in all the models (Eqs. (2)–(4). This is best seen in the case of cloud area regression models (Eqs. (3) and (4), where the model exponent a_1 (denoting the effect of N) is by an order of magnitude larger than exponents a_2 and a_3 (denoting effects of d and Q, respectively).

9. Conclusions

A multiparametric study of the pin disc rotational generator of hydrodynamic cavitation (RGHC) was performed to evaluate the effects of the geometric characteristics of the rotor–stator design at various operating conditions. 17 rotor–stator instances with the following characteristics were studied under 3 operating conditions: diameter, number and shape of rotor pins, and distance between rotor and stator pins. Evaluation of both hydrodynamic performance and cavitation conditions was carried out on the test rig where pressure and energy characteristics were measured and cavitation was described by simultaneous visualisation and pressure fluctuation measurement. A cavitation cloud detection algorithm was developed and run over all the studied instances (approx. 2.5 million frames) to determine the time series of the cavitation cloud area, which was used in combination with the acoustic pressure and its power spectra to interpret the mechanisms of cavitation generation and fluctuation dynamics. For most cases, amplified peaks occur at the rotational and pin-pass frequencies, while a broader amplified band between 500 and 1000 Hz occurs only in cases where cavitation is present. The 8 pin 6.5 mm diameter case stands out with a discrete frequency of 547 Hz that correlates with cloud collapse. In contrast, the NACA 0500 case and the one without a stator are characterised by a very weak spectral response due to the absence of cavitation. Simultaneously acquired pressure and cavitation cloud images could not be directly correlated due to the complexity of the pressure field caused not only by the dynamics of cloud collapse near the hydrophone in the view plane of the camera, but throughout the entire chamber. The raw imaging data and processed pin pass sequences are available in the supplementary.

Mutual instance comparison was performed on the basis of pressure head, power consumption, rms value of acoustic pressure p_{RMS} average value of cavitation cloud area A_{AVE} and its standard deviation A_{STD}. A significant correlation was found between the cavitation extent, given as A_{STD} and the exerted p_{RMS} value, indicating that hydrophone pressure measurement is an effective tool for cavitation monitoring. Following the comparison, the effects of the number, diameter, and shape of the pins were determined:

1. Higher number of pins has a suppressing effect on the development, elongation and collapse of the cavitation cloud, which is due to the absence of space behind the pin in which a low pressure wake is formed.
2. Higher pin diameter has a favourable effect on the extent of cavitation and pumping ability at the expense of higher power consumption. The instance with 4 mm pins was found to be unsuitable and the one with 6.5 mm was found to be the most suitable for further investigation.
3. Cylindrical and triangular pointed 70° pins were found to be of interest, while others such as blunt triangle, heart-shaped and especially NACA 0500 pins were found to be not beneficial. Further investigation of triangle length and inclination with respect to hydrodynamic performance would be interesting.

The effects of flow rate, rotor pin diameter, and number of rotor pins were quantified using a regression model that shows the dom-

inance of the effect of pin number, which is in the case of the A_{AVE} and A_{STD} regression models about 10 times larger than pin diameter and flow rate. The stator and rotor–stator distance were found to play an important role, as the case without stator resulted in significantly lower p_{RMS}, A_{AVE} and A_{STD} values compared to the other cases. Interestingly, a shortening of the rotor–stator gap distance enhances the fluctuation of the cavitation cloud only up to a certain distance, while a higher p_{RMS} value was measured at a distance of 1.75 mm than at a distance of 0.25 mm.

Based on the results of the study, further work will be directed toward experiments with contaminated liquid samples to evaluate the efficiency in terms of geometric and operational properties. Furthermore, additional geometric properties such as the number of rotor pins below 8, the number and diameter of stator pins, and the volume of the housing chamber will be investigated using the p_{RMS}, A_{AVE} and A_{STD} evaluation tools developed in this study.

Declaration of Competing Interest

The authors declare that they have no known competing financial interests or personal relationships that could have appeared to influence the work reported in this paper.

Acknowledgements

The authors would like to thank the University of Ljubljana for the financial support within the UL Innovation Fund, acknowledge the financial support from the European Research Council (ERC) under the European Union's Framework Program for research and innovation, Horizon 2020 (grant agreement n°771567 — CABUM) and the Slovenian Research Agency (research projects No. J2-3057, L7-3184 and J7-2601 and research core funding No. P2-0401 and P2-0422).

Appendix A. Supplementary data

Supplementary data to this article can be found online at https://doi.org/10.1016/j.jestch.2022.101323.

References

[1] F.J. Simmons, I. Xagoraraki, Release of infectious human enteric viruses by full-scale wastewater utilities, Water Res. 45 (12) (2011) 3590–3598, https://doi.org/10.1016/j.watres.2011.04.001.
[2] F. Barancheshme and M. Munir, 'Strategies to combat antibiotic resistance in the wastewater treatment plants', Front. Microbiol. 8, 2018, Accessed: Aug. 12, 2022. [Online]. Available: https://www.frontiersin.org/articles/10.3389/fmicb.2017.02603.
[3] N. Mehle, M. Ravnikar, Plant viruses in aqueous environment – Survival, water mediated transmission and detection, Water Res. 46 (16) (2012) 4902–4917, https://doi.org/10.1016/j.watres.2012.07.027.
[4] R.K. Singh, L. Philip, S. Ramanujam, Disinfection of water by pulsed power technique: a mechanistic perspective, RSC Adv. 6 (15) (2016) 11980–11990, https://doi.org/10.1039/C5RA26941E.
[5] B. Wang, H. Su, B. Zhang, Hydrodynamic cavitation as a promising route for wastewater treatment – A review, Chem. Eng. J. 412 (2021), https://doi.org/10.1016/j.cej.2021.128685 128685.
[6] D. Panda, V.K. Saharan, S. Manickam, Controlled hydrodynamic cavitation: A review of recent advances and perspectives for greener processing, Processes 8 (2) (2020) 220, https://doi.org/10.3390/pr8020220.
[7] M. Yadav, J. Sharma, R.K. Yadav, V.L. Gole, Microbial disinfection of water using hydrodynamic cavitational reactors, J. Water Process Eng. 41 (2021), https://doi.org/10.1016/j.jwpe.2021.102097 102097.
[8] M. Badve, P. Gogate, A. Pandit, L. Csoka, Hydrodynamic cavitation as a novel approach for wastewater treatment in wood finishing industry, Sep. Purif. Technol. 106 (2013) 15–21, https://doi.org/10.1016/j.seppur.2012.12.029.
[9] B. Maršálek, Š. Zezulka, E. Maršálková, F. Pochylý, P. Rudolf, Synergistic effects of trace concentrations of hydrogen peroxide used in a novel hydrodynamic cavitation device allows for selective removal of cyanobacteria, Chem. Eng. J. 382 (2020), https://doi.org/10.1016/j.cej.2019.122383 122383.
[10] X. Sun et al., Disinfection characteristics of an advanced rotational hydrodynamic cavitation reactor in pilot scale, Ultrason. Sonochem. 73 (2021), https://doi.org/10.1016/j.ultsonch.2021.105543 105543.
[11] X. Sun et al., Multi-objective optimization of the cavitation generation unit structure of an advanced rotational hydrodynamic cavitation reactor, Ultrason. Sonochem. 80 (2021), https://doi.org/10.1016/j.ultsonch.2021.105771 105771.
[12] J. Vilarroig, R. Martínez, E. Zuriaga-Agustí, S. Torró, M. Galián, S. Chiva, Design and optimization of a semi-industrial cavitation device for a pretreatment of an anaerobic digestion treatment of excess sludge and pig slurry, Water Environ. Res. 92 (12) (2020) 2060–2071, https://doi.org/10.1002/wer.1366.
[13] L.M. Cerecedo, C. Dopazo, R. Gomez-Lus, Water disinfection by hydrodynamic cavitation in a rotor-stator device, Ultrason. Sonochem. 48 (2018) 71–78, https://doi.org/10.1016/j.ultsonch.2018.05.015.
[14] B. Širok, M. Dular, and M. Petkovšek, 'Cavitation device for treatment of water by cavitation', US20160167983A1, Jun. 16, 2016 Accessed: Nov. 16, 2021. [Online]. Available: https://patents.google.com/patent/US10202288B2/en?inventor=sirok&oq=sirok
[15] M. Petkovšek, M. Zupanc, M. Dular, T. Kosjek, E. Heath, B. Kompare, B. Širok, Rotation generator of hydrodynamic cavitation for water treatment, Sep. Purif. Technol. 118 (2013) 415–423.
[16] M. Petkovšek, M. Mlakar, M. Levstek, M. Stražar, B. Širok, M. Dular, A novel rotation generator of hydrodynamic cavitation for waste-activated sludge disintegration, Ultrason. Sonochem. 26 (2015) 408–414, https://doi.org/10.1016/j.ultsonch.2015.01.006.
[17] T. Stepišnik Perdih, B. Širok, M. Dular, On the bubble-surfactant interaction, Chem. Eng. Process. 121 (2017) 198–204, https://doi.org/10.1016/j.cep.2017.08.016.
[18] J. Gostiša, M. Zupanc, M. Dular, B. Širok, M. Levstek, B. Bizjan, Investigation into cavitational intensity and COD reduction performance of the pinned disc reactor with various rotor-stator arrangements, Ultrason. Sonochem. 77 (2021) 105669.
[19] J. Gostiša, B. Širok, S.K. Repinc, M. Levstek, M. Stražar, B. Bizjan, M. Zupanc, Performance evaluation of a novel pilot-scale pinned disc rotating generator of hydrodynamic cavitation, Ultrason. Sonochem. 72 (2021) 105431.
[20] J. Gostiša, P. Drešar, M. Hočevar, and M. Dular, 'Computational analysis of flow conditions in hydrodynamic cavitation generator for water treatment processes', Can. J. Chem. Eng. p. cjce.24572, Jul. 2022, 10.1002/cjce.24572.
[21] T. Klinger, Image Processing with LabVIEW and IMAQ Vision, Prentice Hall Professional, 2003.
[22] I. Sobel and G. Feldman, *An Isotropic 3x3 Image Gradient Operator*. 2015. 10.13140/RG.2.1.1912.4965.
[23] R.W. Fox, P.J. Pritchard, A.T. McDonald, Introduction to Fluid Mechanics, John Wiley & Sons, 2010.
[24] M. Petkovšek, M. Hočevar, P. Gregorčič, Surface functionalization by nanosecond-laser texturing for controlling hydrodynamic cavitation dynamics, Ultrason. Sonochem. 67 (2020), https://doi.org/10.1016/j.ultsonch.2020.105126 105126.
[25] P. Kumar, D. Chatterjee, S. Bakshi, Experimental investigation of cavitating structures in the near wake of a cylinder, Int. J. Multiph. Flow 89 (2017) 207–217, https://doi.org/10.1016/j.ijmultiphaseflow.2016.09.025.